

Project Title: One-click sample alignment in electron microscopy

Report Due: 10/10/2022 Received: 10/10/2022

Specific Confidentiality requirements: None

Academic Supervisor: Nick Brooks

Main industrial Supervisor: Christopher Allen

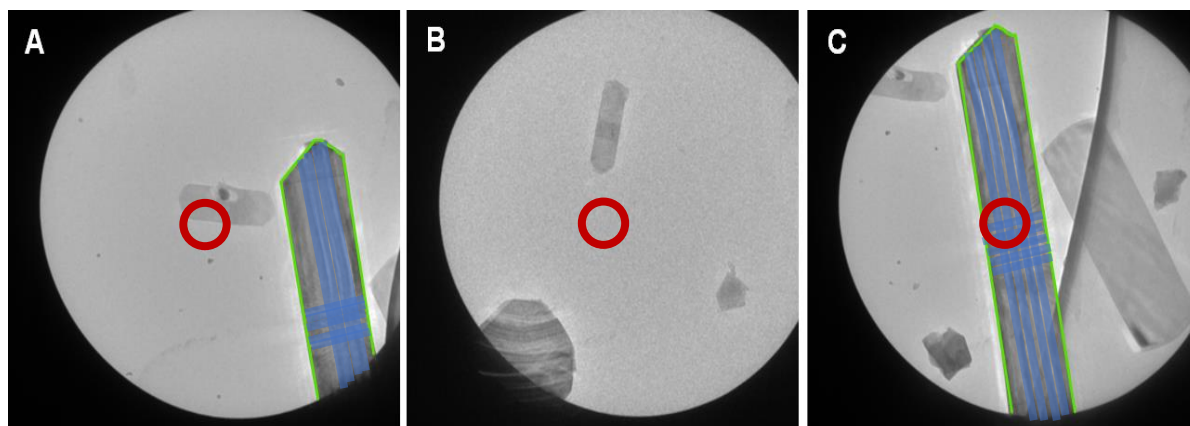
Co-industrial Supervisor: Timothy Poon

Abstract:

When imaging beam-sensitive samples, such as perovskites, MOFs and supramolecular crystals, prolonged exposure to the electron beam can lead to the sample's crystal structure breaking down [5-7]. In particular, knock-on damage and radiolysis can be major contributors to structural changes at high and low accelerating voltages, respectively [4]. Therefore, all processes which require illumination of the sample should be completed while minimising electron fluence. However, obtaining high-resolution STEM images of single crystals typically requires the sample to be oriented onto a high symmetry zone axis. This is achieved using the Kikuchi diffraction patterns as a roadmap to orient the sample, where the bands form from diffuse inelastic scattering of electrons in the sample and connect high symmetry zone axes. Due to the patterns varying for different crystal systems, finding the correct zone axis can be difficult in some cases. One specific challenge is that large tilts may be required, which can quickly cause the user to lose track of their position and hinder their ability to find which zone axis corresponds to the desired orientation. Moreover, predicting the correct stage correction after a tilt requires parameters unique to a specific sample holder and microscope combination.

This work aims to create scripts in Digital Micrograph to automate the process of sample orientation to a specific zone axis [13]. The scripts allow a user to reorient a sample on a double-tilt holder given an image containing Kikuchi bands. This is done by either manually clicking on a zone axis within the image or via using line detection algorithms in Python to find a specific zone axis. This was tested on a JEOL ARM300CF, where the resulting pixel shifts a zone axis underwent after a tilt was first measured. The stage shifts were then calculated by modelling a tilt to be about a pivot point, correcting for shift errors such as backlash using scaling parameters unique to a sample holder and microscope combination. These unique parameters can be rapidly determined using provided helper scripts. Future works would then include the possible zone axes being determined and displayed to allow a

user to traverse freely between zone axes.



Diffraction space images of MoO_3 nanocrystals at 300 kV, where the centre of the optic axis is marked by a red circle. (A) shows a crystal, outline in green, oriented off zone. The zone axis should be moved to within the red circle. (B) shows the image after tilting, where the crystal of interest has moved outside the field of view. (C) show how, after automated stage position correction, the crystal returns to the centre of the imaged with the beam now oriented on the zone axis.

Introduction:

Transmission Electron Microscopy (TEM) is an incredibly useful tool for characterising organic and inorganic materials, allowing users to obtain a vast array of information such as the crystal structure, topology, and compositional and chemical environments of the material [1]. This is done via accelerating electrons within the microscope and then focussing them using electrostatic and magnetic lenses into a coherent beam onto the sample. These electrons are then scattered by the sample and can be collected to produce atomic resolution images, as shown in Figure 1 where Scanning Transmission Electron Microscopy (STEM) was utilised [2, 3].

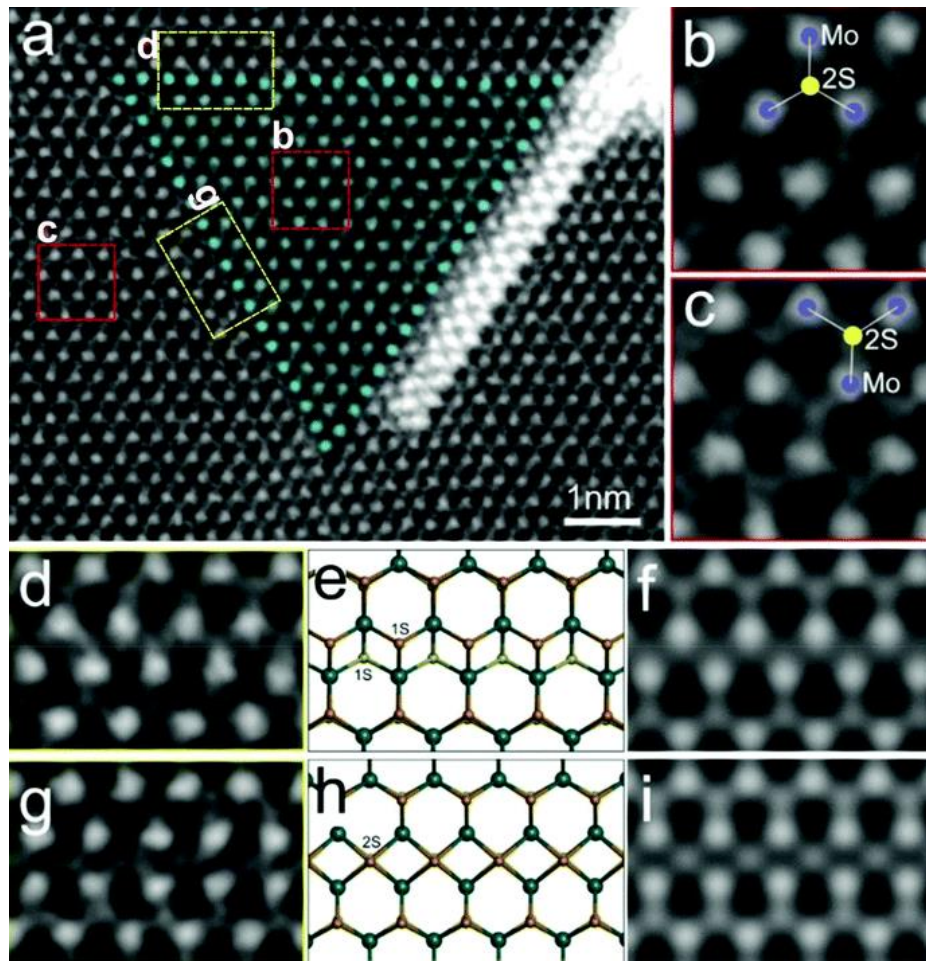


Figure 1, (a) Atomic resolution STEM image of a MoS₂ monolayer. (b, c) are magnified views of the regions highlighted in (a) and show the inverted lattice orientations of MoS₂. (d, g) are magnified views of the regions highlighted in (a) and show the two types of boundary structures present. (e, h) are the respective atomic models and (f, i) are the respective simulated STEM images [3].

However, the inelastic collisions that produce these images can lead to electron-beam damage. This damage to the sample can cause the structure or chemistry to change the longer the sample is exposed, making interpretation of the produced images more difficult as the specimen is no longer representative of the material. [2] Knock-on damage and radiolysis are 2 major contributors to this structural damage. In the case of radiolysis, this is when the inelastic scattering breaks the chemical bonds of the material where lower accelerating voltages make this more common. This is particularly damaging to specific ceramics, minerals, and most polymers. Conversely, knock-on damage is caused by the displacement of atoms from the crystal lattice due to the direct transfer of the electron energies to the atoms. This is

commonly seen in metals, however, all samples will suffer from knock-on damage if the accelerating voltage is increased high enough. This greatly limits our ability to image beam-sensitive samples, as beam damage can occur at all electron beam energies. [2, 4]

This issue is clearly seen in several highly researched materials. Examples are perovskites for high-efficiency solar cells, MOFs for catalysis, and supramolecular crystals for drug encapsulation. For each of these beam-sensitive samples, the structures are easily damaged during the process of imaging which has led to high-resolution imaging being one of the most difficult applications of TEM [5, 6, 7]. Therefore, to minimise the effects of beam damage, it is necessary to minimise the amount of exposure the sample has to the electron beam, reducing the rate of radiolysis and knock-on damage.

This is made difficult as obtaining high-resolution STEM images of single crystals requires the electron beam to be oriented down the sample's atomic columns, also known as a zone axis. This is shown in Figure 2.

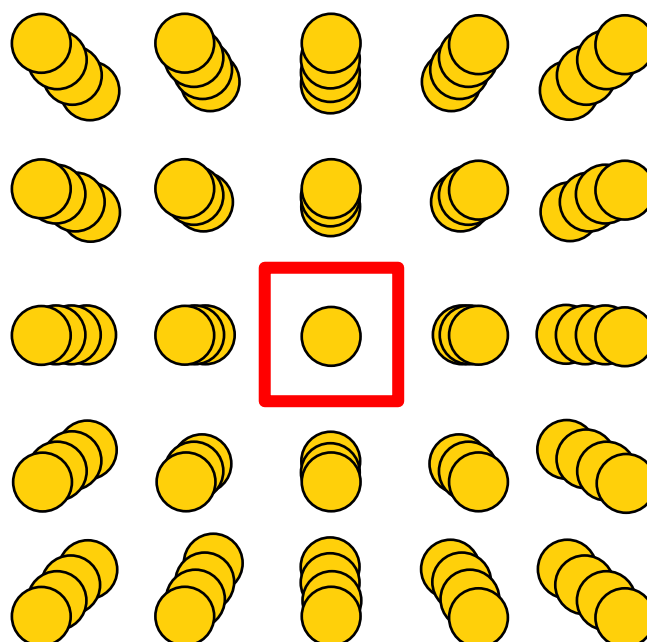


Figure 2, Viewing down the zone axis of a crystal, where each yellow circle represents an atom. The red box shows the view when looking directly down a stack of atoms.

As it is not possible to directly see the direction to rotate the crystal from a STEM image, it is necessary to be able to determine the direction via alternate means. A particularly useful method is to look at the diffraction patterns produced from the sample.

Diffraction is classically described as occurring when waves reflect off adjacent scattering centres with a path difference equal to an integral number of wavelengths. This condition allows for the waves to constructively interfere and will only occur when the waves are reflected at the Bragg angle, as shown in Figure 3 [2].

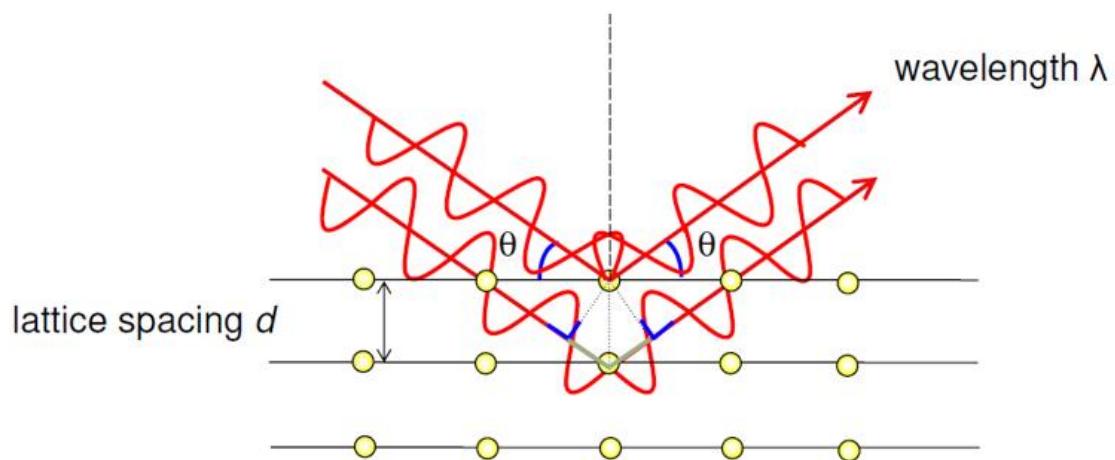


Figure 3, Bragg description of diffraction, showing the reflection of a wave with wavelength λ incident at an angle θ to atomic planes of spacing d . θ is the Bragg angle of diffraction [8].

Applying this to a crystal exposed under an electron beam of wavelength comparable to the atomic spacing, only reflections that satisfy the Bragg angle appear in the form of spots that represent a particular crystal lattice plane. It is then possible to determine you are at a zone axis by rotating the sample until the diffraction pattern looks symmetrical, as shown in Figure 4.

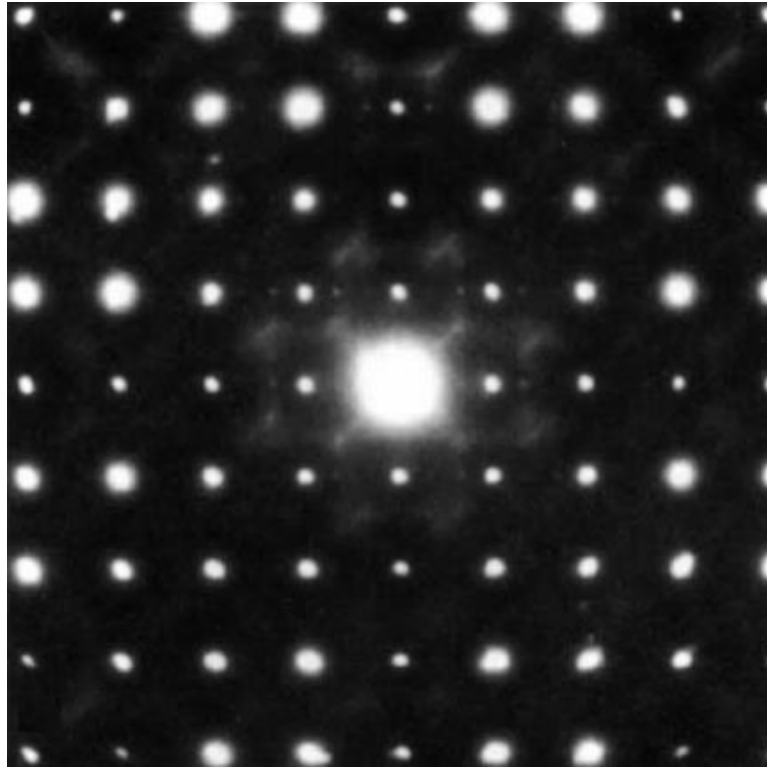


Figure 4, Electron diffraction pattern of a $\text{Nb}_4\text{W}_{13}\text{O}_{49}$ crystallite along the $[001]$ zone axis. The symmetry present when looking along the zone axis is displayed [9].

Bragg spots however have limited practical use as a guide to finding the zone axis due to the rotation of the sample also varying the intensities of the spots, making it difficult to accurately determine when you are at the zone axis. Instead, with a thicker sample it is possible to look at Kikuchi lines. These are formed when the electrons first scatter diffusely within the sample and then those that satisfy the Bragg angle of diffraction will undergo a second inelastic scattering. As the scattered electrons are travelling in all directions due to the initial diffuse scattering, the direction of the electrons that undergo the secondary scattering varies. Therefore, unlike in Figure 4, 2 cones form from electrons scattered under Bragg conditions. This will result in bands appearing, as shown in Figure 5 [10].

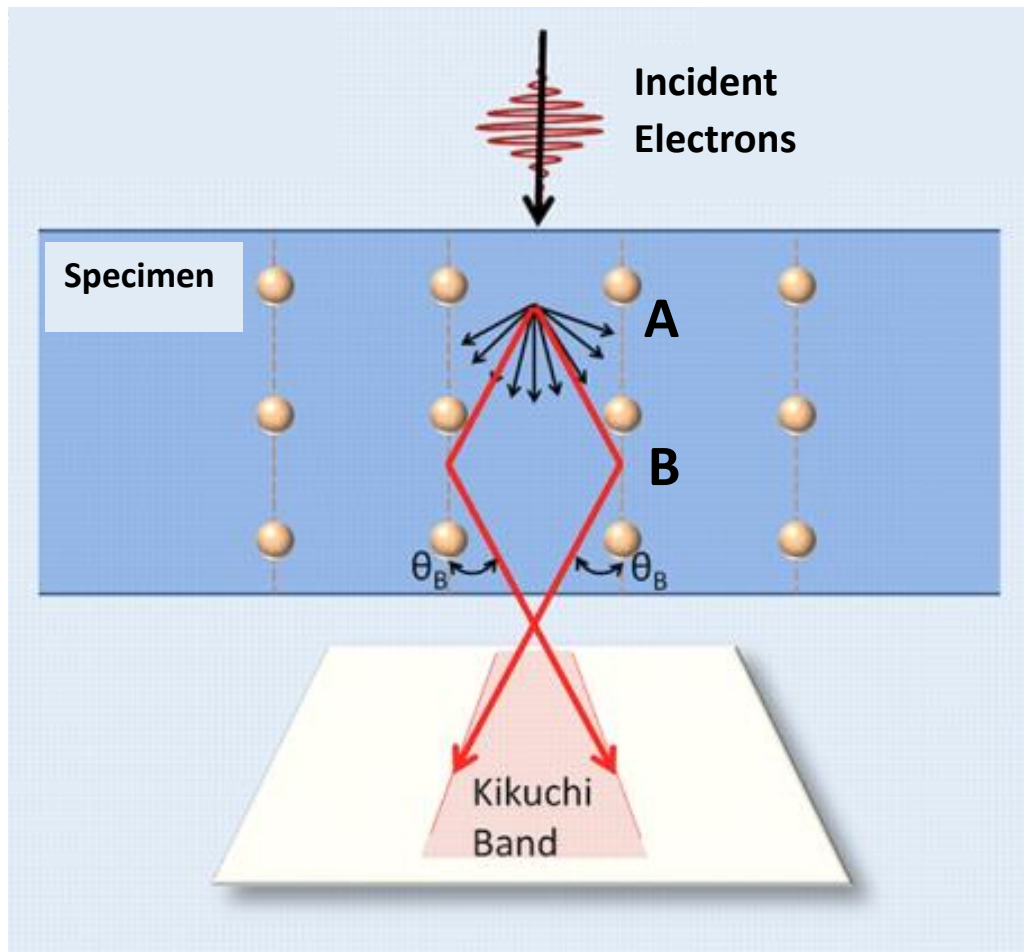


Figure 5, Schematic outlining the formation of Kikuchi bands. (A) The incident electrons undergo an initial scattering in all directions. (B) The diffusely scattered electrons then undergo Bragg diffraction. Due to the electrons reflecting off the lattice planes from all directions whilst satisfying the Bragg angle, a cone of inelastically scattered electrons forms. These cones then interact with the viewing screen to produce Kikuchi bands. Figure adapted from [11].

Kikuchi diffraction patterns present a given zone axis as being the intersection of bands, where different zone axes are connected by bands. It is possible to then navigate to different zone axes by rotating the sample and following the bands. Most importantly, rotating the crystal does not affect the intensity of the pattern. These patterns produced by the sample are therefore typically used as a roadmap to navigate between zone axes. This is shown in Figure 6 [10].

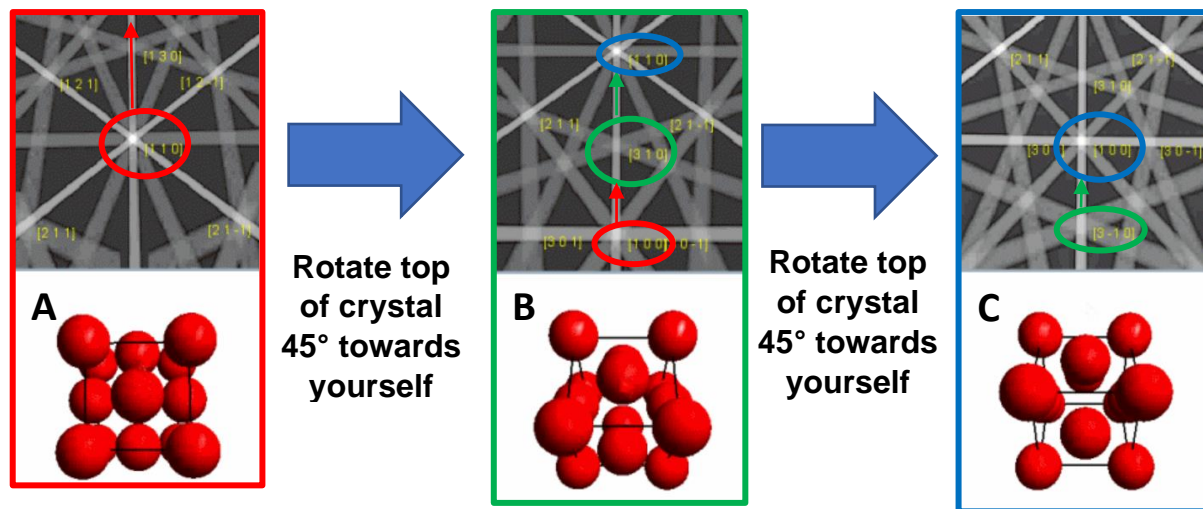


Figure 6, A Face Centred Cubic (FCC) crystal being rotated 90° alongside simulated Kikuchi diffraction patterns. The symmetry of each zone axes is also labelled. (A) A high symmetry zone axis, $[1\ 1\ 0]$ within the red circle, looking directly down the face of the crystal. (B) Rotating the crystal 45° leads to a low symmetry zone axis, $[3\ 1\ 0]$ within the green circle, where the rotation has caused the viewed Kikuchi diffraction pattern to move up along the band indicated by a red arrow. It can be seen how looking directly down (B)'s atomic columns do not show a well-defined overlap of atoms. (C) Rotating a further 45° leads to a new high symmetry zone axis, $[1\ 0\ 0]$ within the blue circle. The view is directly down the edges of the crystal, where the viewing image moved up along the green arrow. It can be seen how high symmetry zone axes demonstrate better atomic stacking whilst also demonstrating the ability to navigate the crystal orientation through Kikuchi diffraction patterns [12].

However, as seen in Figure 6, it can be difficult to determine when at a high symmetry zone axis. For example, in orientation B the beam is looking down the $[3\ 1\ 0]$ zone axis however the arrangement of atoms has low symmetry. Due to the low symmetry, the stacking of the atoms is not well defined and therefore a lower-resolution image would be produced. This is made more complicated as the Kikuchi diffraction patterns vary for different crystal structures.

A second major difficulty arises from how tilting a sample in the microscope can lead to the sample moving outside of the viewing image. This can lead to a user having to spend time relocating the crystal, as shown in Figures 7 - 8. Whilst the same tilt is done in both Figures, the magnitude and direction of the stage shift are different. This is clearly seen in how the magnitude of the Z stage shift needed to return to focus is 20 μm different and they occur in different directions. Notably, the only significant difference in the regions tilted is that they were viewed at different X stage values. A 5° tilt is also relatively small, where a user may have to tilt anywhere up to

30°. Given that a user may be attempting to image nanocrystals, even a relatively small tilt can shift the viewed image in the micrometres and can lead to the region of interest being difficult to find due to the stage's non-linear behaviour.

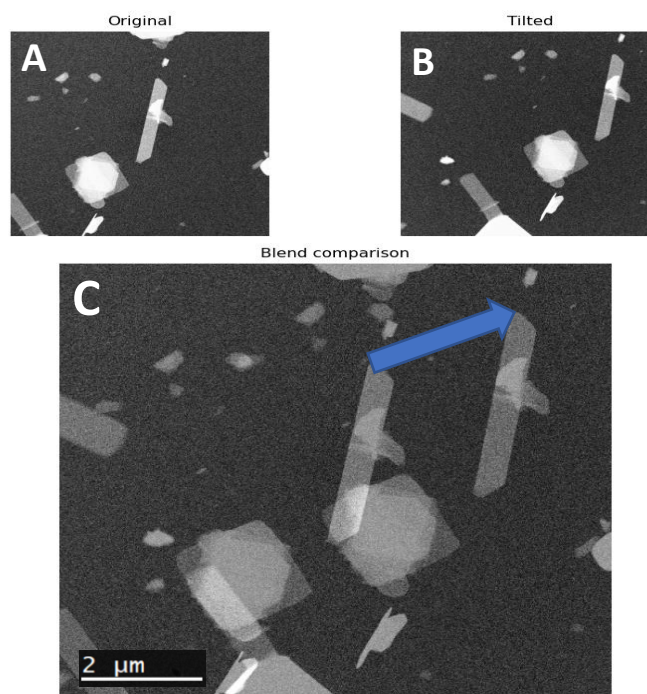


Figure 7, Image comparison of MoO₃ nanocrystals that have undergone a β tilt from 0 to 5° when viewing the stage at $X = -22 \mu\text{m}$, $Y = 21 \mu\text{m}$ on the JEOL ARM300F at Diamond Light Source Ltd. (A) The sample at 0°, where $Z = -84 \mu\text{m}$. (B) The sample after applying a β tilt of 5°, where Z is increased to $-51 \mu\text{m}$ to return to focus. (C) Blend comparison of (A) and (B), where the crystal has moved to the upper right by approximately $3.1 \mu\text{m}$.

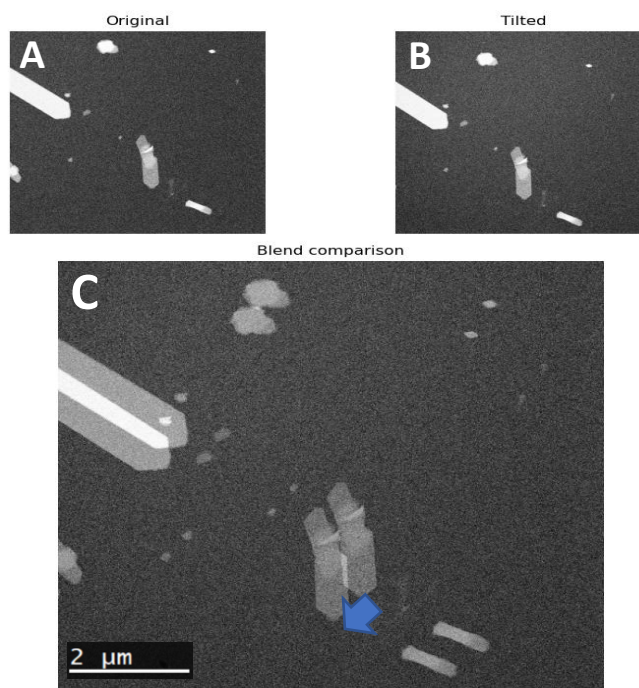


Figure 8, Image comparison of MoO_3 nanocrystals that have undergone a β tilt from 0 to 5° when viewing the stage at $X = 677 \mu\text{m}$, $Y = 33 \mu\text{m}$ on the JEOL ARM300F at Diamond Light Source Ltd. (A) The sample at 0°, where $Z = -89 \mu\text{m}$. (B) The sample after applying a β tilt of 5°, where Z is decreased to $-120 \mu\text{m}$ to return to focus. (C) Blend comparison of (A) and (B), where the crystal has moved to the lower left by approximately $0.6 \mu\text{m}$.

The difficulty finding a high symmetry zone axis coupled with the regions of interest shifting whilst making the tilts leads to reaching the conditions for a high-resolution STEM image is a significant challenge even for an experienced user. This causes the sample to be exposed to the beam for a prolonged period and undergo beam damage. Therefore, having the ability to predict the necessary tilts needed to orient the sample such that the electron beam is parallel to a high symmetry zone axis, followed by calculating the required stage shifts to move the region of interest back into view would drastically decrease the amount of time the sample is exposed. This not only saves time for users but will also reduce the amount of damage caused to the sample when attempting to meet the conditions necessary for a high-resolution STEM image. Furthermore, this can be used alongside additional tools to help image beam-sensitive samples, such as setting the microscope conditions to minimise the beam damage that the sample is most prone to, leading to a cumulative benefit.

Creation of software to enable such automated tilting and stage shift correction needs to be compatible with most microscopes, being something that can be

installed within a pre-existing suite that is already being used to aid microscope control. The suite should also allow the user to communicate with the microscope, retrieving information on the stage as well as being able to rotate and shift the stage on command. An example of software that has these features built-in whilst also being well-known and widely used for TEM is Digital Micrograph™ (DM) by Gatan Inc. [13].

Whilst DM has recently made it possible to create scripts in Python, allowing access to the vast array of existing Python libraries, this feature is not present in earlier versions of DM such as v2.x. As most microscopes are set up to be compatible with a specific version of DM, some will not have access to versions that have Python as a hosted language. Instead, DM features an in-built scripting language similar to C++ that has been used in the creation of numerous programs, from simple image filtering to automated image acquisition. Between DM versions, there are slight changes in the functions defined within the scripting language, however the creation of a program for automated tilting and stage shift correction written in the scripting language would allow a greater range of compatibility with microscopes. Any issues related to untested DM versions should be relatively easy to solve compared to writing a separate program for Python-capable microscopes [14].

Therefore, this work aims to create scripts in DM to automate the process of sample orientation to a specific zone axis. This is to create an interface that is widely compatible with most microscopes capable of STEM imaging which can be used to reduce beam damage on samples when attempting to reach the necessary conditions for high-resolution imaging. This would allow for better quality images to be obtained for many beam-sensitive samples while also reducing the time required to obtain a good image.

Aims and Objectives

The first objective was to create an interface that allows a user to click on a zone axis within the image. The required tilts to move the zone axis to be parallel to the beam would be applied, and then the stage shift corrections needed to return the region of interest into the field of view would be made. This interface should be written in DM's scripting language to allow compatibility with microscopes using any

version of DM. Achieving this would create the base interface needed to allow for automated tilting of a zone axis and can be applied not only to obtaining high-resolution STEM images, but also to techniques where a user is viewing an object on a stage that must be significantly tilted.

Next, additional DM scripts should be made to allow for easy determination of all relevant parameters needed for the interface to be able to function. This should allow for the parameters to be determined should the interface be used on a new microscope or when recalibrating due to microscope conditions changing. Examples would be if the electron beam's energy is changed or if a new sample stage holder is used. Once completed, this would ensure that the interface can be set up for any microscope that allows for a sample to be tilted with 2 degrees of freedom.

Third, fully automate the detection of a zone axis within an image. This would allow the interface to become fully automatic given that the relevant calibration data is known and removes the need for a user to specify the location of a zone axis.

Lastly, be able to determine zone axes outside of the viewing image that are also within the tilt range of the microscope. This should also include the determination of the symmetry labels for each zone axis. Completion of this would allow a user to have full control over how they want to view the sample and would drastically decrease the time needed to acquire high-resolution STEM images of a particular area of a sample (such as looking down the pores of a zeolite).

Additionally, all stage movements should be done mechanically. This is due to the default location of the beam being set such that the electron beam is as close to the microscope's optic axis as possible. Altering the beams' location changes this and can lead to the image's resolution being affected.

Lastly, all objectives should ideally be achieved within DM, however it is possible to interface DM with Python. This would allow access to the vast array of Python libraries without jeopardising the utility of the interface.

Methodology

To allow for complete control over the location of the zone axis, it is assumed that the microscope can tilt the sample in 2 orthogonal directions. In the case of the JEOL ARM300F, this is achieved via the TEM's goniometer (α -tilt) alongside a sample stage holder capable of tilting orthogonally to the goniometer (β -tilt). This is shown in Figure 9.

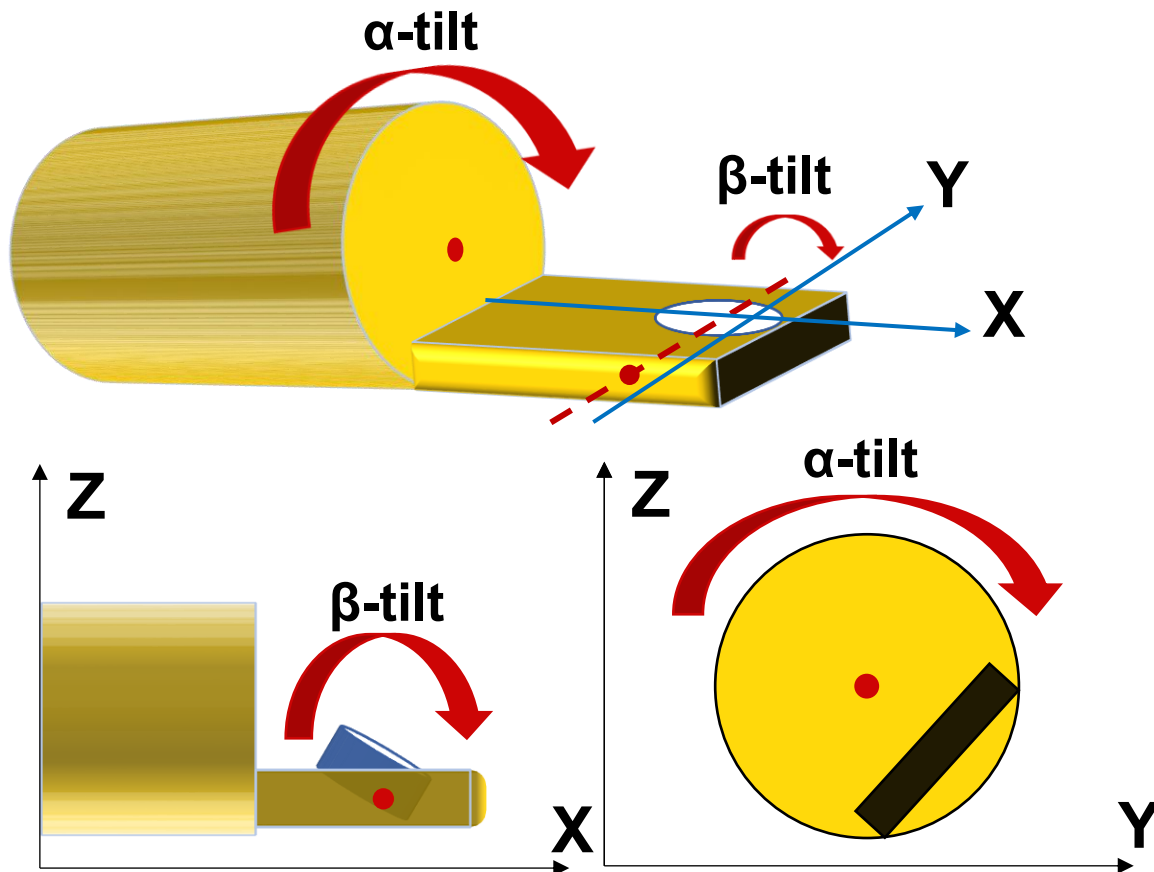


Figure 9, Schematic showing how a typical electron microscope tilts. For both an α and β tilt, there is a defined point of rotation marked by a red circle. The specimen is within the white circle. An α tilt is done by the goniometer and is approximately restricted to the YZ plane, where the tilt axis can be defined at some (Y, Z) coordinate. A β tilt is done by the sample holder and is approximately restricted to the XZ plane, where the tilt axis can be defined at some (X, Z) coordinate.

The tilts shown in Figure 9 can be described geometrically by defining a pivot point about which the sample rotates about. This is shown for a β tilt in Figure 10.

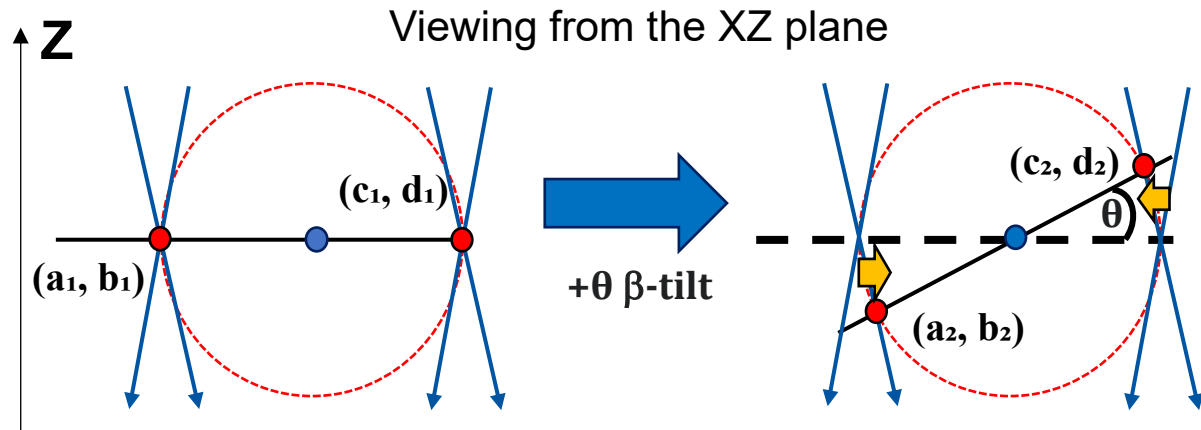


Figure 10, Schematic showing how a β tilt can be geometrically represented. Blue arrows represent an electron beam, where a pair intersect at the location on the sample which is being viewed. These regions of interest are represented by red circles. The pivot point for the tilt is represented by a blue circle. After a tilt is applied for a given region of interest, (a_1, b_1) or (c_1, d_1) , they will rotate about the pivot point. As the electron beam's location is not changed, a shift in the viewing image will occur. Given the tilt cannot exceed $\pm 90^\circ$, the direction shifted is only dependent on the X stage position of the region of interest whilst the magnitude varies depending on the change in tilt made. It is assumed that the distance between the region of interest and the pivot point is much greater than the distance between the XY plane the sample sits on and the XY plane of the pivot point.

Looking at the regions of interest in Figure 10, the magnitude and direction of the shift resulting from a tilt is dependent on the location of the region of interest relative to the pivot point. A larger distance will cause a larger overall shift, whilst the magnitude of the shift in X and Z depends on the location the region of interest is moved between on the circle. This relationship can be described as shown in (1) and (2) for the new X and Z stage positions, respectively.

$$c_2 = c_1 \cos(\theta) - d_1 \sin(\theta), \quad (1)$$

$$d_2 = c_1 \sin(\theta) + d_1 \cos(\theta) \quad (2)$$

Given that the pivot point is defined to be at $(0,0)$, the position of the region of interest, (c_1, d_1) , after a tilt, θ , is defined to be at (c_2, d_2) . It is also assumed that a positive rotation moves counterclockwise. Notably, as the position of the region of interest approaches the location of the pivot point, the subsequent shift tends to 0.

Whilst this indicates that a solution to the stage shifting problem would be to use crystals as close as possible to the pivot point, this is rarely practically feasible. Reducing the distance between the region of interest and the pivot point also leads to the assumption that the difference in Z between the region of interest and pivot

point being negligible no longer holding. This alters the stage-shifting behaviour, as shown in Figure 11.

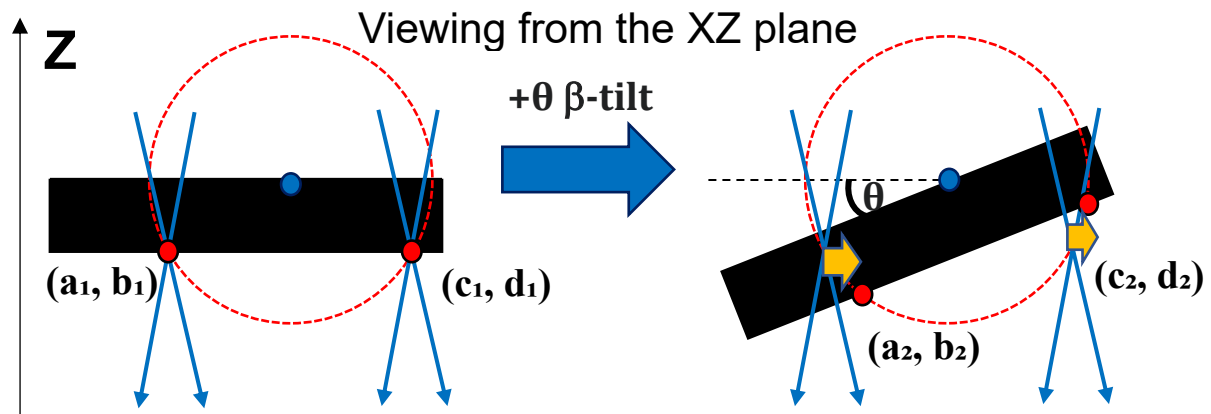


Figure 11, Schematic showing a β tilt as described in Figure 10, however the Z distance between the pivot point and the region of interest is not negligible. Comparing two regions of interest on each side of the pivot point, the direction of the shifts is now in the same direction rather than the opposite.

Therefore, it is ideal to solve the stage shifts generally to remove any limitations on how close the region of interest is to the pivot point. Using this simple geometric model, the shifts can be accurately determined. To be able to solve for this stage shift as outlined in Figure 10, the tilt made, initial position of the region of interest, and pivot point must be known.

Tilting:

Given that the location to move a Kikuchi zone axis to be in line with the beam could be anywhere on the screen, 2 degrees of rotational freedom are necessary.

Determining the tilt needed to shift the zone axis to given locations can be done by first measuring the pixel shifts of a zone axis associated with the tilt. This should ideally be done for $\pm 10^\circ$ for each tilt, where a given tilt could be associated with both an x and y pixel shift [15]. Once this is repeated for each tilt, the relationship between a given tilt and the resulting pixel shifts can be defined as shown in equations (3) to (6).

$$Y = A\alpha \quad (3)$$

$$Y_c = B\beta \quad (4)$$

$$X = C\beta \quad (5)$$

$$X_c = D\alpha \quad (6)$$

Y and Y_c are the Y pixel shifts of a zone axis after undergoing an α and β tilt, respectively. X and X_c are the equivalent X pixel shifts. A, B, C and D are the scaling constants determined via calibration. It is assumed that $Y > Y_c$ and $X > X_c$, where an α tilt primarily causes a Y pixel shift whilst a β tilt primarily causes an X pixel shift. When $Y_c = X_c = B = D = 0$, the image axis perfectly matches the sample tilt axis.

Once the location the zone axis must be moved to is known, the pixel shifts necessary, X and Y , can be found. The minimum values of α and β can then be determined iteratively. First, the smallest possible value of a tilt, β in this case, is directly calculated. As (5) assumes that $C > B$, a β tilt mainly causes an X pixel shift, so the smallest necessary value for a β tilt would be (7).

$$\beta = \frac{X}{C} \quad (7)$$

As the β tilt may then result in a Y pixel shift, expression (8) finds the remaining Y pixels that the zone axis must travel.

$$Y_{dif} = Y - Y_c = Y - B\beta \quad (8)$$

Using the remaining Y pixels, (9) determines the necessary α tilt to move the zone axis towards the desired location.

$$\alpha = \frac{Y_{dif}}{A} \quad (9)$$

As the α tilt may also result in a small X pixel shift, (10) determines the remaining X pixels to move.

$$X_{dif} = X - X_c = X - D\alpha \quad (10)$$

Substitute X_{dif} into (7) in place of X and continue to solve expressions (7) to (10) until the change in tilt per iteration is below a defined threshold. Should the tilt axis match the image axis, $Y_c = X_c = 0$, and therefore $Y_{dif} = Y$, $X_{dif} = X$. This will lead to the tilts being calculated exactly within the first iteration.

Given the location of the beam's focal point is known and if the location of a zone-axis is given, the required tilts to move the zone-axis to be parallel to the beam can therefore be calculated. The location of the zone-axis can be entered manually, by clicking on the image or even by automatic detection as the only information required is the relative pixel location from the beam's focal point.

Region of interest's initial position:

Whilst it is possible to acquire the position of the region of interest on the sample stage through DM, it is necessary to make sure that the frame of reference used remains unchanged between sessions. This requires having a reference point that will remain invariant regardless of whether the sample stage holder is removed and reinserted into the microscope. This would allow for a single pivot point to be able to describe the rotations made.

This can be particularly difficult as, whilst the α tilt axis is fixed by the goniometer, moving the sample position in XYZ will move the sample stage within the goniometer. As the β tilt axis is fixed to the sample stage, there would be no set relationship between the β and α axis positions. To account for the lack of a reference point for a β tilt axis, the methodology outlined in Figure 12 is used.

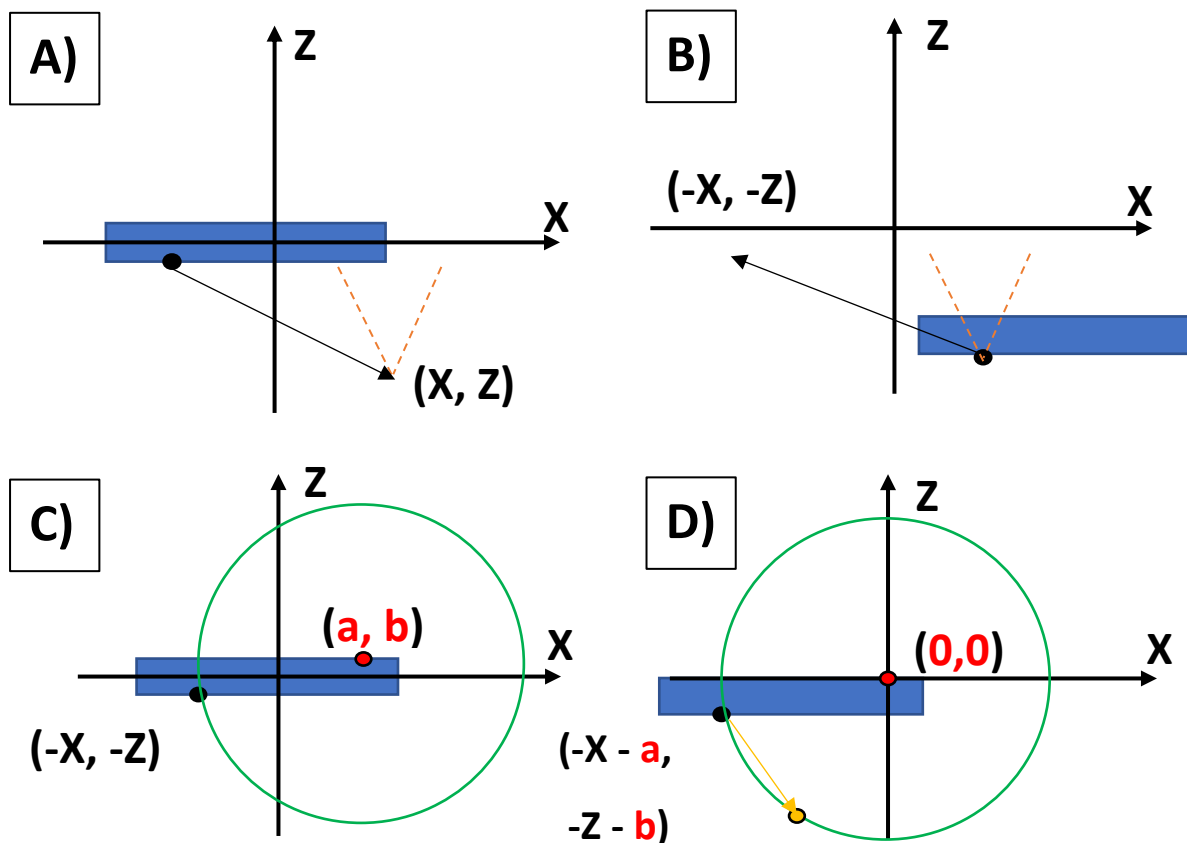


Figure 12, Method for determining the initial position of a β tilt. When the stage is inserted into the microscope, the same point on the stage will be defined as the origin within some random error. Assuming the region of interest is within the black circle, this must be shifted to the location of the electron beams' focal point outlined as a dashed orange point. This will occur via some X and Z stage shifts as shown in (A). Once the user has the region in view, the stage is returned to the frame of

reference when the sample had initially entered the microscope. This is calculated by stating the stage would move in the opposite direction, placing the region of interest at $(-X, -Z)$ as shown in (B). This frame of reference, (C), will not be affected by stage shifts and can then be used to determine a unique pivot point, (a, b) capable of describing the tilting behaviour. To reach the conditions for equations (1) and (2) to apply, shift the region of interest by the pivot point and reach (D). The initial positions for a β tilt are therefore $(-X - a, -Z - b)$.

Notably, Figure 12 assumes that a β tilt only occurs in the XZ plane as outlined in Figure 10 and that the point on the stage set as $(0, 0)$ by the goniometer is invariant. This can then be done for an α tilt, as shown in Figure 13. The process for finding the initial position is simpler due to the goniometer remaining fixed by the microscope.

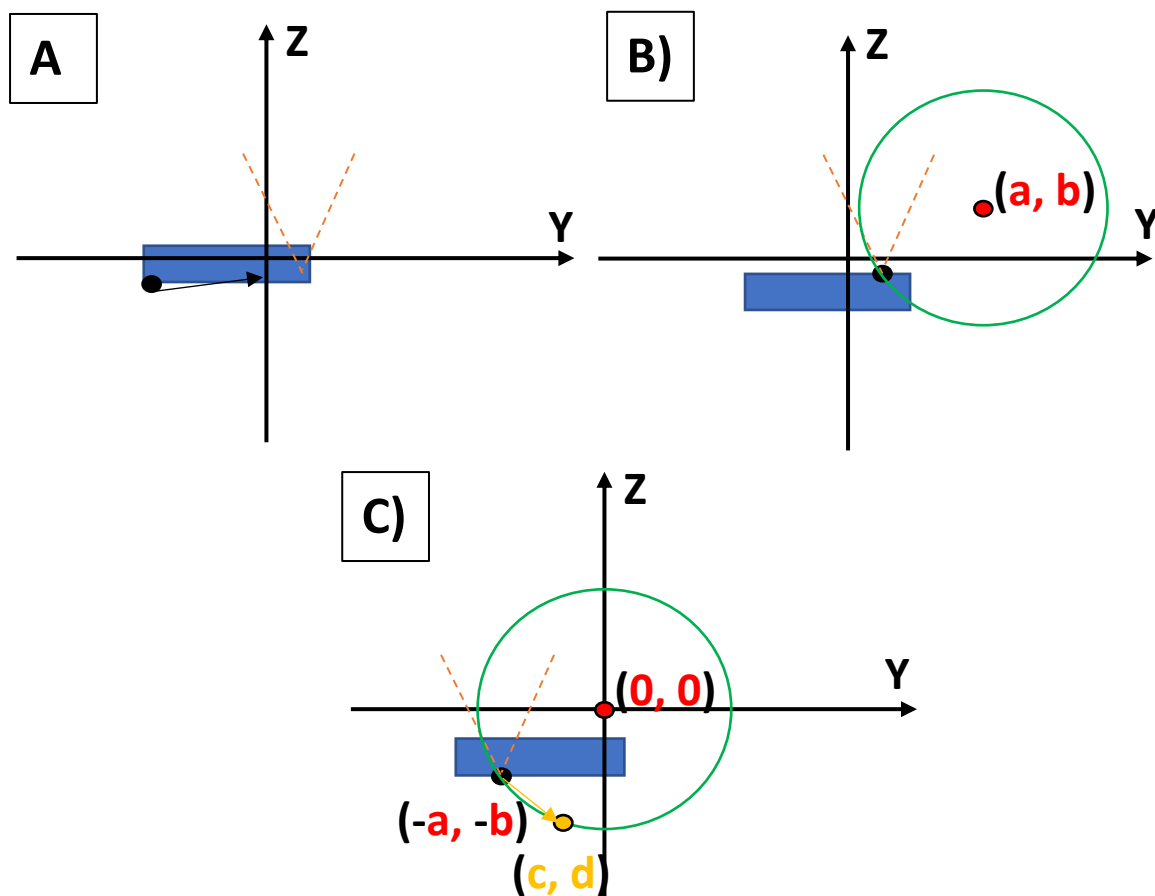


Figure 13, Method for determining the initial position of an α tilt. When the stage is inserted into the microscope, it is assumed that the focal point of the electron beam is not changed. Assuming the region of interest is within the black circle, this must be shifted to the location of the electron beams' focal point outlined as a dashed orange point in (A). As the location where the region of interest will be viewed within the goniometer will always be the same, information on the stage position is not needed. Once the user has the region in view, the positions can then be shifted by the determined pivot point, (a, b) , to reach the conditions needed for equations (1) and (2), shown in (C). The initial positions for an α tilt are therefore $(-a, -b)$.

The method to reach the initial positions for an α tilt assumes that the electron beam's focal point position remains invariant throughout use. This is typically true as the manufacturer would set default settings for ideal imaging conditions using the microscope. Whilst there is the ability to alter the Z height of the focal point via altering lens strengths, it should be assumed that this is not done for this assumption to hold. Similarly, it is approximated that the tilt purely occurs in the YZ plane.

These 2 methods therefore allow for the initial positions to be determined for the 2 types of tilts typically present. However, these values are dependent on the pivot point which must be first found.

Pivot Point:

Determination of a pivot point was found to best be done iteratively. This is done by applying a given tilt and then, using a guess value for the pivot point's coordinates, calculating the expected stage shift correction needed. If the location moved to does not match how the region of interest was before tilting, move the stage until they match. The stage positions that the microscope should have moved to can then be retrieved and the pivot point necessary to do this rotation can be calculated. This process is then repeated until the change in pivot points calculated converges below a threshold. This is outlined in Figures 14 - 15.

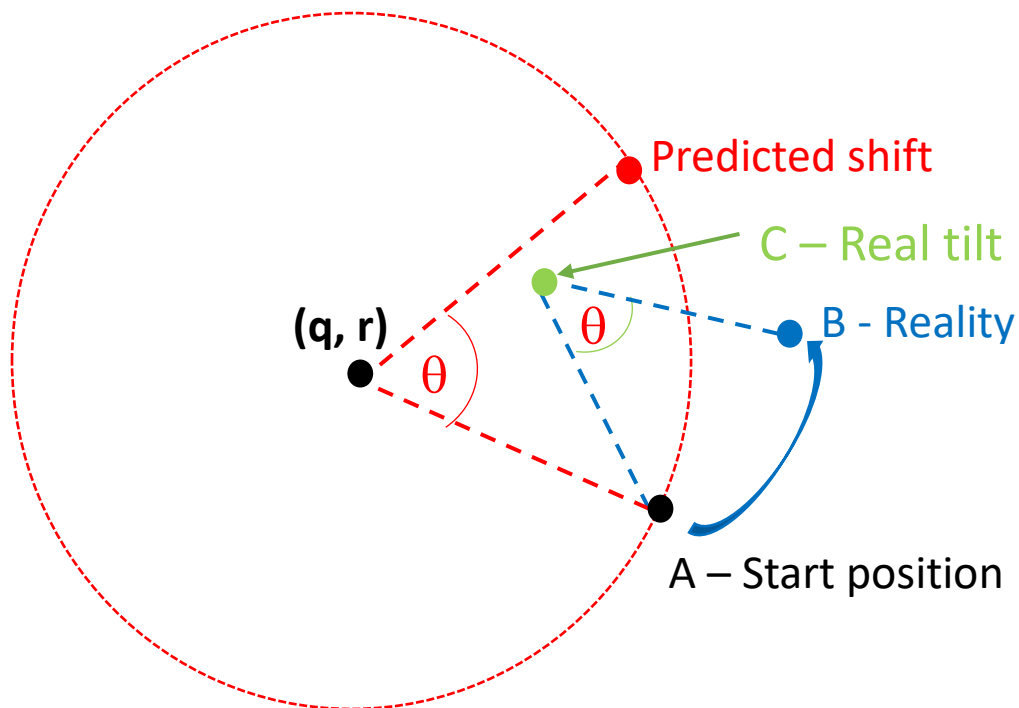


Figure 14, Iterative method to converge to a tilt's pivot point. θ is the tilt applied, (q, r) is a guess pivot point and A is the position before tilting. A would be found as outlined in Figures 12 – 13. The predicted shift is the location A is expected to move based on θ and (q, r) using the method outlined in Figure 10. B is the actual stage position once the region of interest is tilted and shifted back into the original view. C represents the 'actual' pivot point needed for the same tilt to move the sample from A to B.

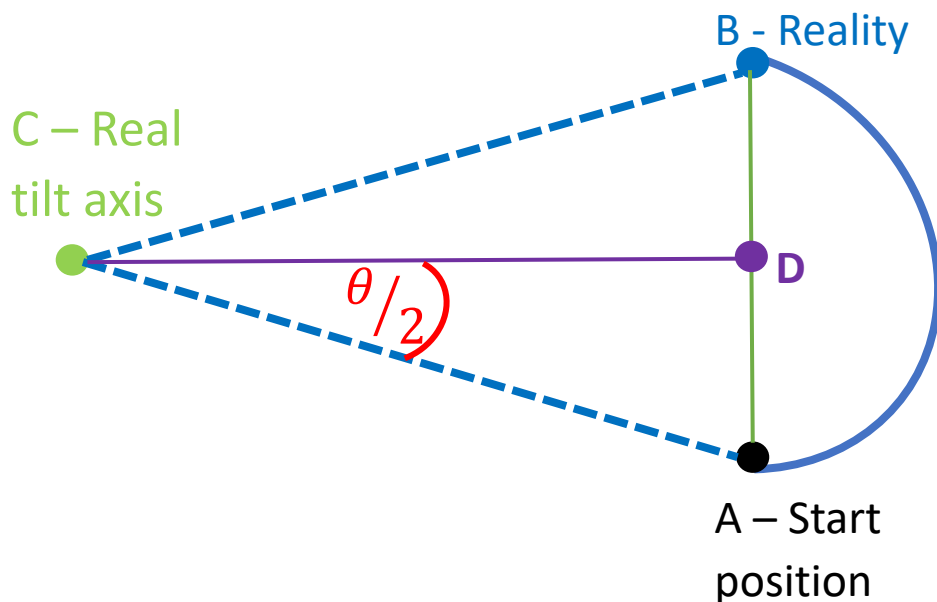


Figure 15, Triangle ABC defined in Figure 14. As angle $\check{C}\check{A}D$ is equal to angle $\check{C}\check{B}D$, two equivalent right-angle triangles are formed when splitting triangle ABC along line CD, where D is the midpoint of line AB. Arc AB could be as drawn, else it could also be in the opposite direction.

A good guess of the pivot point is needed for this method to work, otherwise convergence will not occur when using the method at different stage positions. This is due to how there are 2 possible solutions for what C could be for a given arc, and only the solution closest to the guessed pivot point is considered. As the arc travelled by the sample is not defined, there are 2 possible arcs, leading to a total of 4 possible solutions. It is possible to acquire an estimate of the pivot point by running 2 tilt series at 2 different locations on the sample.

Using these 3 methods, it is possible to acquire all the required information to predict the tilt needed to move the zone-axis to be parallel to the beam, followed by the subsequent stage shift corrections.

Experimental Calibrations:

All scripts were written in DM version 3.22.1461.0, where 20 functions and classes were coded across approximately 2000 lines. These were then tested on the JEOL ARM300F located at Diamond Light Source Ltd. UK where the resulting calibrations are shown.

Tilt calibration:

A Si [110] sample was used to determine the parameters needed to solve equations (3) to (6). This sample was chosen as it was not beam-sensitive and is a standard sample used to calibrate TEMs. The results of the tilt calibration are shown in Figure 15.

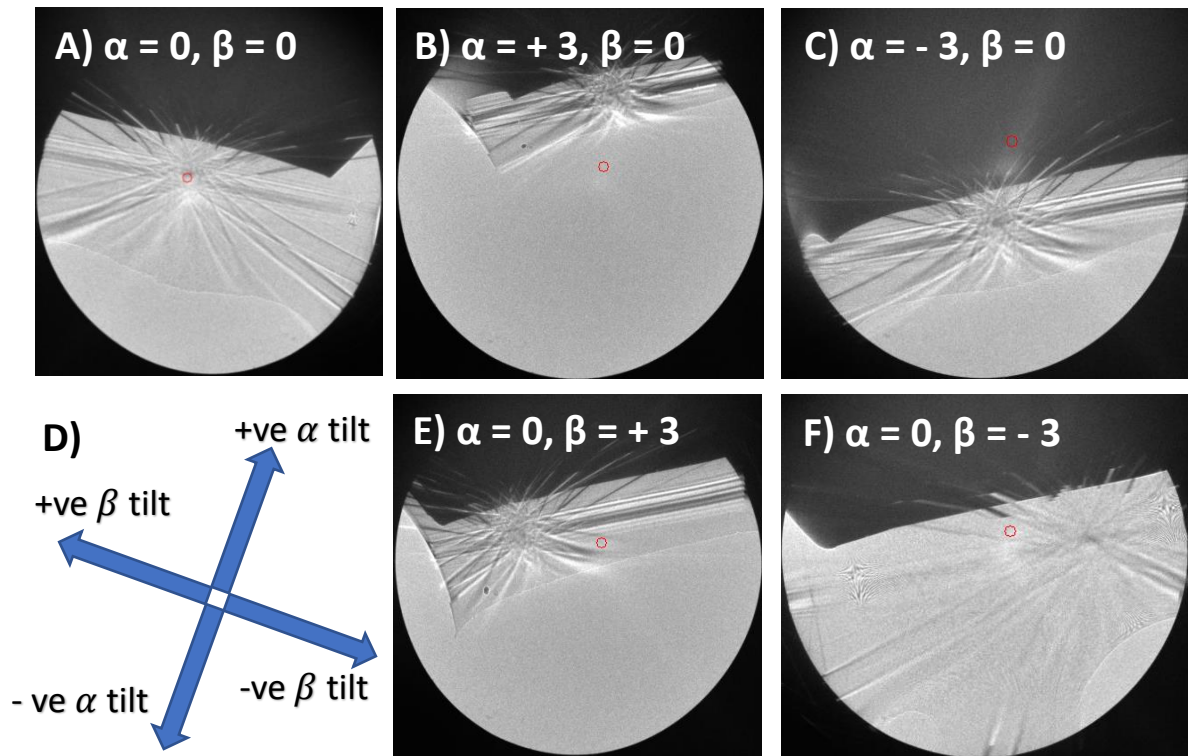


Figure 16, Tilt calibration using Si [1 1 0] on the JEOL ARM300F with a double tilt stage holder (EM-31630) based at Diamond Light Source Ltd. UK. Beam energy was set to 300 kV, camera length to 20 cm and the images were 4096 by 4096 pixels. (A) Zone axis when no tilts have been made, where the centre is defined by a red circle. (B) Zone axis after a $+3^\circ$ α tilt. (C) Zone axis after a -3° α tilt. (E) Zone axis after a $+3^\circ$ β tilt. (F) Zone axis after a -3° β tilt. (D) Directions moved by the zone axis after each tilt variation was applied.

It was found that whilst changing the camera length and image size will similarly alter the pixels a zone axis will move for a given tilt, the constants can be scaled linearly based on the values used during the calibration. This led to the values of the scaling constants being $A = -110.361$, $B = 15.2638$, $C = -119.28$ and $D = -17.5$ in pixel/degree when using a 4096 by 4096 image with a camera length of 8 cm.

Pivot point calibration:

The pivot points for both an α and β tilt were then found using the method outlined in Figure 14. An example of the method being used is seen in Figure 16 for an α tilt. It can be seen how the magnitude of the correction was wrong by more than $4 \mu\text{m}$ initially but quickly converges to a minimum within 3 iterations.

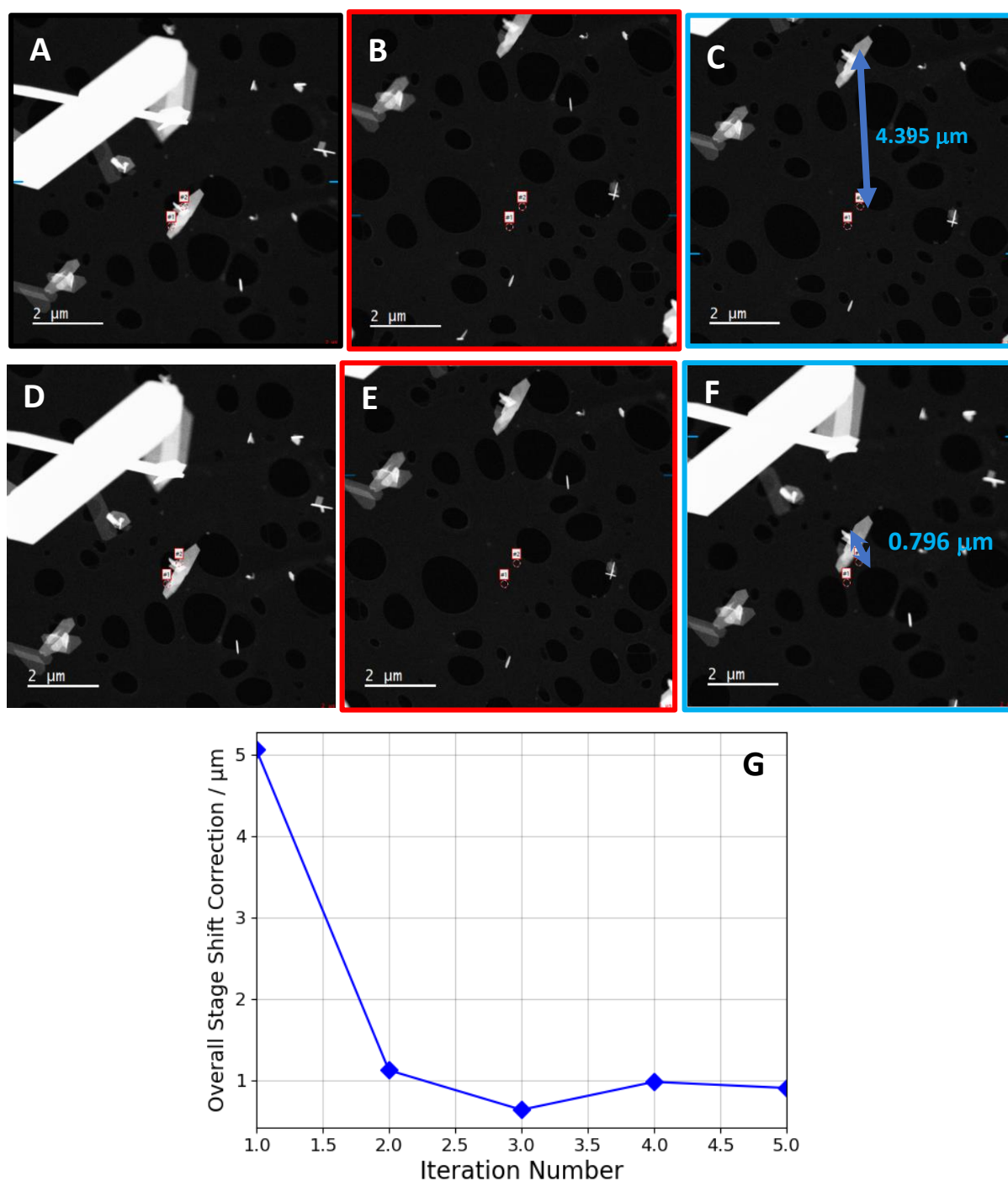


Figure 17, α tilt axis position calibration using MoO_3 nanocrystals on the JEOL ARM300F with a double tilt stage holder (EM – 31630) based at Diamond Light Source Ltd. Beam energy was set to 300 kV, camera length to 9 cm and the images were 2048 by 2048 pixels. (A, B, C) The first iteration of the calibration, where the initial viewing image, the image after a 3° α tilt, and the image after the calculated stage shift correction has been applied are respectively shown. The initial guess for the pivot point was $Y = 26$, $Z = 11$ μm . Comparing (A) to (C) shows that the stage shift correction was off by 4.4 μm in the XY plane. (D, E, F) The fifth iteration of the calibration, where the initial viewing image, the image after a 3° α tilt, and the image after the calculated stage shift correction has been applied are respectively shown. Comparing (D) to (F) shows that the stage shift correction was off by

0.8 μm , where the final pivot point was determined to be at $Y = 12.8$, $Z = 97.6 \mu\text{m}$. (G) The rate of convergence to the pivot point can be seen when viewing the amount the stage shift was off by in (X, Y, Z) after every iteration. After 3 iterations, the error converges to a number above 0.

From Figure 9.G, it can be seen that the error in stage shift correction did converge to a value greater than 0. This is likely due to errors in stage shifts as well as hysteresis arising from the mechanical motors used to move the stage.

Backlash and hysteresis calibration:

To incorporate hysteresis and any remaining errors associated with shifting, scripts were made to monitor the movement of an object within the image and compare it with the movement the microscope claims to have moved. This was done by commanding the microscope to continually do $0.5 \mu\text{m}$ shifts in a given direction, then comparing the movement made by the object of interest via a phase cross-correlation. The difference between the inputted stage shift and the actual stage shift was then represented as shown in expressions (11) and (12) where scaling constants S_X and S_Y were defined.

$$(X \text{ inputted}) \times S_X = (X \text{ moved by microscope}) \quad (11)$$

$$(Y \text{ inputted}) \times S_Y = (Y \text{ moved by microscope}) \quad (12)$$

It was found that S_X and S_Y are dependent on the previous stage shifts made, where the more you move in the same direction, the closer the constants are to 1. This is due to backlash caused by the gaps in the mechanical cogs used to move the stage and can be modelled simply via an exponential plateau. This is shown in equation (13), where parameters M , a and b are needed to predict stage shift errors.

$$y = M(1 - e^{-(ax+b)}) \quad (13)$$

The variables are rapidly calibrated in an automated fashion for each direction by running multiple stage shift series and running a phase cross-correlation to determine the actual shifts. This was done for both X and Y stage shifts, which were then fitted via (13), as shown in Figure 18.

Using these fits, it can be determined how much a given shift should be scaled. An example for an X stage shift of $+3.3 \mu\text{m}$ would require first determining where the stage currently is on the curve. This is done by having a stage logger in the background monitoring the magnitude and direction the stages have shifted. Assuming the most recent X stage movements were $+4 \mu\text{m}$, then starting from $4 \mu\text{m}$

on the curve defined by (13), apply shifts in $0.5 \mu\text{m}$ increments where the amount communicated to the microscope should be scaled up by S_x at each step. The final $0.3 \mu\text{m}$ can be treated to behave the same as a $0.5 \mu\text{m}$ shift. Given that the stage shifts may not purely occur in the stated direction, such as an X stage shift also causing a small Y shift, the method can also be applied to determine the error associated. This is by defining the real direction moved as an angle from the defined stage axis.

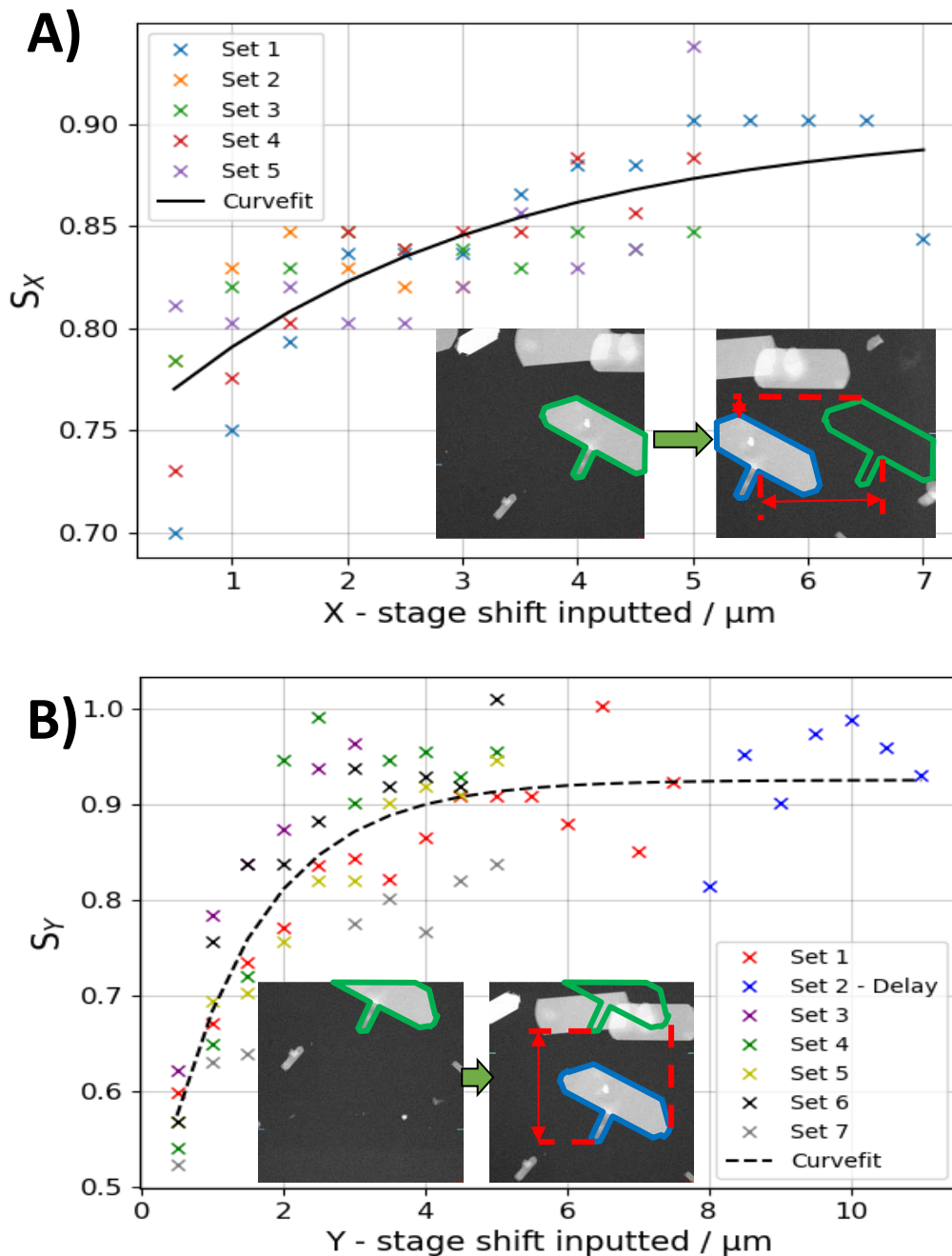


Figure 18, S_x and S_y change when applying stage shifts in $0.5\ \mu\text{m}$ increments having moved $5\ \mu\text{m}$ in the opposite direction before the measurements. 5 sets of X stage movements were plotted and a curve fit using expression (13) was done in (A), whilst (B) shows 7 sets of Y stage movements and the subsequent curve fit. In (B), Set 2 directly occurred after Set 1, where a 5-minute delay was made, and no movements were done during the delay. In both plots, the scaling parameters do not converge to 1 as would be expected if the error was purely hysteresis.

Using the curves outlined in Figure 18, backlash arising due to mechanical movements can then be predicted as well as errors in communicating movements between the microscope and the stage.

Results

A Graphical User Interface (GUI) was created to contain all relevant scripts for calibration alongside the scripts to use the calibrations to predict the necessary tilts and stage shift corrections needed to align the zone axis with the electron beam whilst keeping the region of interest within the viewing image. Assuming the beam's focal point in the microscope is not changed for a given beam energy and that the stage holder is not damaged in a way that will shift the tilt axis, users can select from a previously calibrated TEM – stage holder pair. This will allow for the necessary tilts and shifts to be found immediately without needing to recalibrate. This required approximately 4000 lines of code, where 8 classes and 39 unique functions and class methods were defined across the scripts. The main GUI is shown in Figure 19, where the 23 calibration parameters and how they are determined are shown.

If the calibration parameters are already known for the particular microscope setup, a user can click on the viewing image to input the beam's focal point and the location of the Kikuchi zone axis. The script can then begin, where the tilt needed to align the 2 will be calculated and applied. Then the stage shift corrections will be applied. During this process, the beam does not need to be on the sample to monitor the changes, and instead can be blanked. This would further reduce possible beam damage.

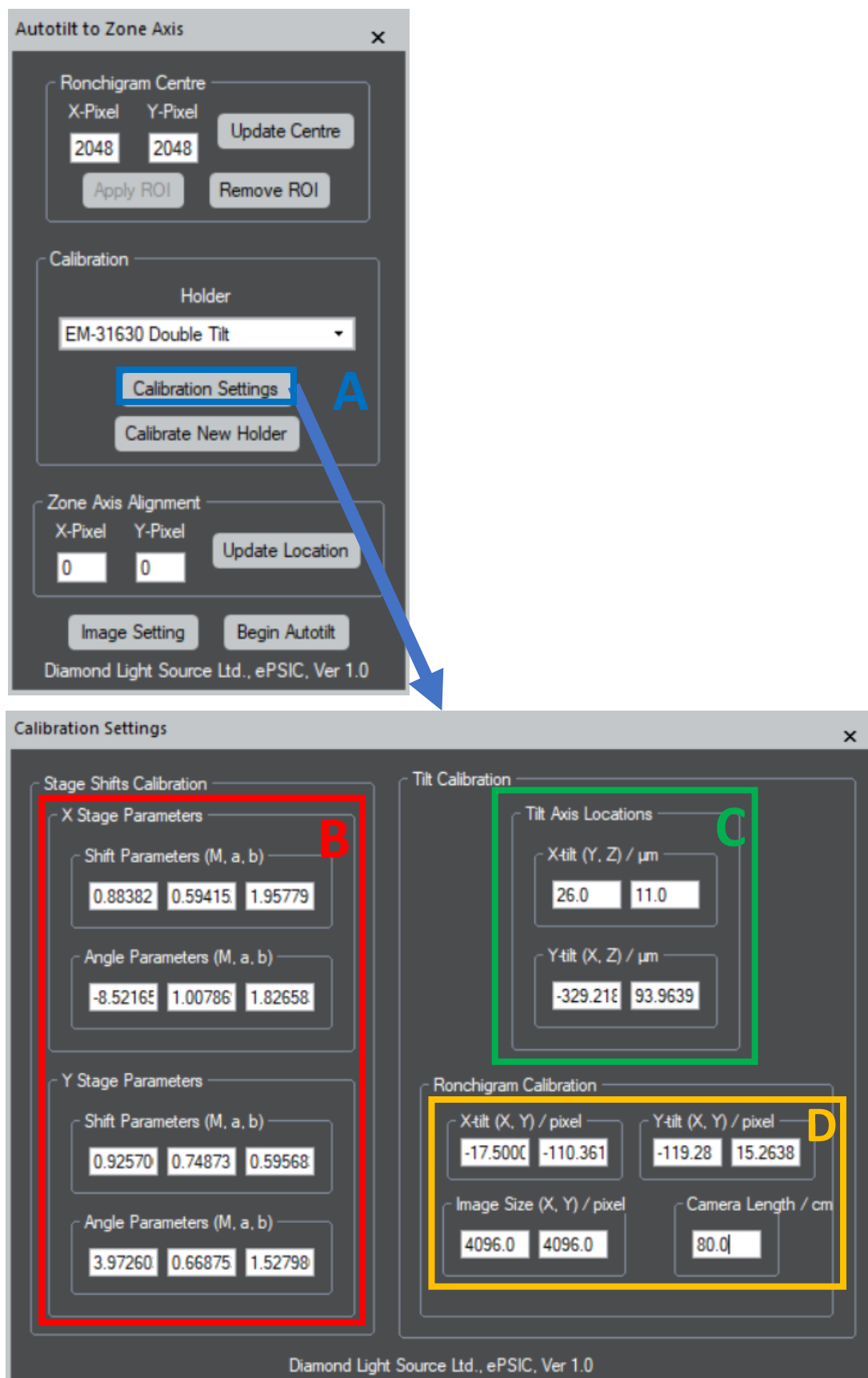


Figure 19, GUI for automated tilting and stage shift correction of a zone axis to be parallel to the electron beam. Once a given calibration set is selected in the dropdown box, (A) can be pressed to

view the calibrated parameters. (B) Stage shifting parameters determined as outlined in Figure 18. (C) Pivot point locations are determined as outlined in Figure 14 – 15. (D) Relationship between a tilt and the pixels a Kikuchi zone axis will move, as shown in Figure 16.

An example of using the script on MoO₃ nanocrystals imaged using the JEOL ARM300F and double tilt holder (EM – 31630) at Diamond Light Source Ltd. UK is shown in Figure 20.

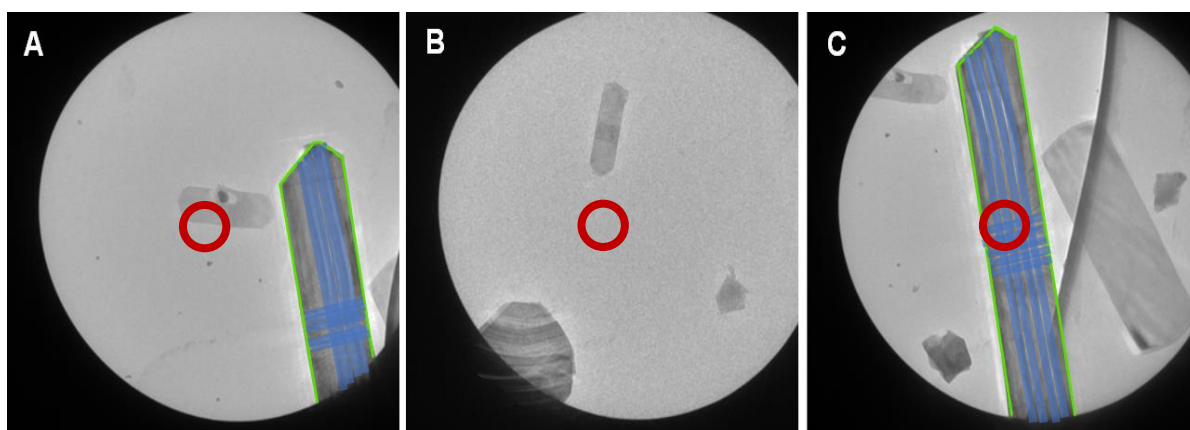


Figure 20, Diffraction space images of MoO₃ nanocrystals at 300 kV, where the centre of the optic axis is marked by a red circle. (A) shows a crystal, outline in green, oriented off zone. The zone axis should be moved to within the red circle. (B) shows the image after tilting, where the crystal of interest has moved outside the field of view. (C) show how, after automated stage position correction, the crystal returns to the centre of the image with the beam now oriented on the zone axis.

Notably, it was found that changing the beam energy to a different preset value would also require the calibration to be redone. This is due to the factory default location for the focal point of the beam changing. Similarly, the rotation of the beam can change, causing the projected diffraction image and STEM images to be rotated. This leads to the direction stage shifts and tilts move changing as well.

Further Automation

The current version of the scripts requires the user to click on the location of the zone axis. Attempts were made to fully automate the detection of zone axes within the viewing image by segmenting the image and then running an autocorrelation on a given segment. This would find the major direction within the segment and, if above a threshold, the direction would be plotted onto a blank binary image [16]. This is shown in Figure 21.

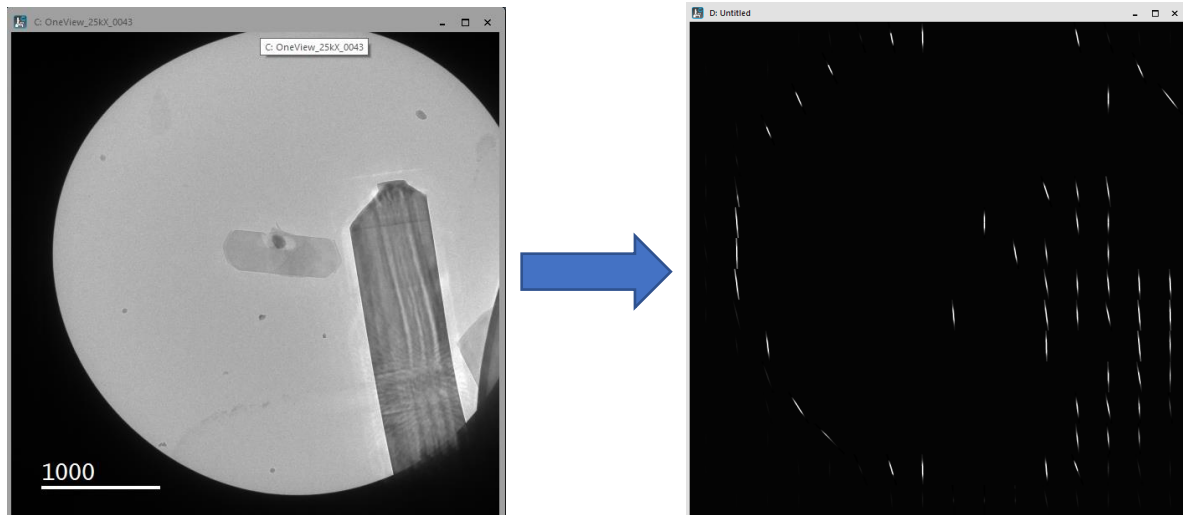


Figure 21, From a 4096 by 4096 diffraction space image, segment into 256 by 256 squares. Each square is then autocorrelated and then the major direction is determined via ellipse fitting. If the direction is significant enough, plot onto a new image otherwise ignore the segment [16].

Once the segmented image was produced, line detection algorithms could be applied where intersections of the lines can be used to flag a zone axis location. The more points of intersection within a given radius, the higher the significance of the detected zone. However, difficulties arose with the segmented image having poor signal due to the complex behaviour of the Kikuchi lines. As seen in Figure 21, the intensity of the lines varies and at times curves. Similarly, the intensity of the crystals vary and can lead to false positives when trying to remove crystal edges from being detected.

An alternative approach was to instead do an atomistic simulation to predict the Kikuchi patterns that would appear. This would require prior knowledge of the crystal lattice as well as requiring an interface between DM and python to allow the simulated Kikuchi diffraction patterns to be matched with the viewing image [17]. Due to the prerequisites on the crystal information as well as difficulties simulating the diffraction patterns within Python, this had not been completed.

Future Work

Given that the initial two objectives were completed, future work would entail automating the detection of zone axes and being able to determine zone axes outside the viewing image.

Automated detection of zone axes can be achieved by continuing to work on either simulating the diffraction patterns and pattern matching the results to the viewing image or by improving the accuracy of line detection and determining the zone axes based on the number of intersections. This would remove the need to click and fully automate the process for tilting and stage shifting the sample.

Determination of zone axes outside the viewing image could be done by extrapolating the previous methods, however new libraries are being made that would allow a user to know all zone axes within the tilt range of the microscope. This could be immediately used alongside the GUI created to allow for the final objective to be completed [15]. In both cases, given the scripts with detailed documentation, Diamond staff will continue to investigate and improve upon the them.

References:

- 1) Mayoral, Alvaro, Paul A. Anderson, and Isabel Diaz. "Zeolites are no longer a challenge: Atomic resolution data by Aberration-corrected STEM." *Micron* 68 (2015): 146-151.
- 2) Williams, David B., and C. Barry Carter. "The transmission electron microscope." *Transmission electron microscopy Vol 1*. Springer, Boston, MA, 1996. 3-17.
- 3) Chen, Jun, et al. "In situ high temperature atomic level dynamics of large inversion domain formations in monolayer MoS₂." *Nanoscale* 11.4 (2019): 1901-1913.
- 4) Egerton, R. F. "Mechanisms of radiation damage in beam-sensitive specimens, for TEM accelerating voltages between 10 and 300 kV." *Microscopy research and technique* 75.11 (2012): 1550-1556.
- 5) Song, Kepeng, et al. "Atomic-Resolution Imaging of Halide Perovskites Using Electron Microscopy." *Advanced Energy Materials* 10.26 (2020): 1904006.
- 6) Liu, Lingmei, et al. "Bulk and local structures of metal–organic frameworks unravelled by high-resolution electron microscopy." *Communications Chemistry* 3.1 (2020): 1-14.
- 7) Olenyuk, Bogdan, et al. "Self-assembly of nanoscale cuboctahedra by coordination chemistry." *Nature* 398.6730 (1999): 796-799.
- 8) Martínez-Ripoll, M. "Crystallography. scattering and diffraction. the bragg's law." *Crystallography-Cristalografia*, Department of Crystallografy & Structural Biology, CSIC, Spain (2022)
- 9) Liao, Yougui. "Practical electron microscopy and database." *An Online Book* (2006).
- 10) Williams, David B., and C. Barry Carter. "The transmission electron microscope." *Transmission electron microscopy Vol 2*. Springer, Boston, MA, 1996. 3-17.
- 11) Yurtsever, Aycan, and Ahmed H. Zewail. "Kikuchi ultrafast nanodiffraction in four-dimensional electron microscopy." *Proceedings of the National Academy of Sciences* 108.8 (2011): 3152-3156.
- 12) Interpreting the diffraction pattern in EBSD. Oxford Instruments. *Miramar Communications Ltd.* (2022)
- 13) Digitalmicrograph software. Gatan Microscopy Suite Software. *Gatan, Inc.* (2022)
- 14) Mitchell, D. R. G., and Bernhard Schaffer. "Scripting-customised microscopy tools for Digital Micrograph™." *Ultramicroscopy* 103.4 (2005): 319-332.
- 15) Olszta, Matthew, and Kevin Fiedler. "Nanocartography: Planning for success in analytical electron microscopy." *arXiv preprint arXiv:2205.03956* (2022).
- 16) Sawada, H., Sannomiya, T., et al. Measurement method of aberration from Ronchigram by autocorrelation function. *Ultramicroscopy*, 108(11), (2008):1467-1475.
- 17) Herron, A.D., et al. Simulation of kinematic Kikuchi diffraction patterns from atomistic structures. *MethodsX*, 5, (2018): 1187-1203.